Bulk Micromachined Titanium Microneedles

E. R. Parker, M. P. Rao, K. L. Turner, C. D. Meinhart, and N. C. MacDonald

***Abstract*—Microneedle-based drug delivery has shown considerable promise for enabling painless transdermal and hypodermal delivery of conventional and novel therapies. However, this promise has yet to be fully realized due in large part to the limitations imposed by the micromechanical properties of the material systems being used. In this paper, we demonstrate titanium-based microneedle devices developed to address these limitations. Microneedle arrays with in-plane orientation are fabricated using recently developed high-aspect-ratio titanium bulk micromachining and multilayer lamination techniques. These devices include embedded microfluidic networks for the active delivery and/or extraction of fluids. Data from quantitative and qualitative characterization of the fluidic and mechanical performance of the devices are presented and shown to be in good agreement with finite-element simulations. The results demonstrate the potential of titanium micromachining for the fabrication of robust, reliable, and low-cost microneedle devices for drug delivery. [2006-0105]**

***Index Terms*—Biomedical engineering, drug delivery systems, microelectromechanical devices, micromachining titanium.**

I. Introduction

MICROFABRICATION techniques have been used for a number of applications in drug delivery, including microneedle arrays capable of painless delivery through the outer layer of the epidermis, the stratum corneum [1], [2]. To date, these microneedle devices have been fabricated using a number of different micromechanical material systems, including silicon [3]–[10], polysilicon [11], [12], polymers [13], [14], and electrodeposited metals [15]–[20]. However, each of these material systems imposes limitations on device performance that ultimately constrain their utility and efficacy. For example, materials such as silicon and glass are intrinsically brittle and polymers possess low elastic moduli and hardnesses. Furthermore, some electrodeposited metals such as nickel are known skin irritants [21]. Consequently, there is a distinct need for the development of additional micromechanical materials to address these shortcomings. Titanium represents one such material.

Owing to its biocompatibility and fracture toughness, titanium has long been used for macroscale biomedical devices such as orthopedic and dental implants [22], [23]. Now, with the advent of enabling micromachining technologies [24], [25], the use of titanium can be expanded into microscale biomedical applications. Using these techniques, micrometer-scale structures with high aspect ratios and vertical sidewalls have been defined in both thick titanium substrates and thin titanium foils via inductively coupled plasma (ICP) dry etching [25]. Thin foil-based microfabrication has proven to be especially advantageous because it allows for the development of three-dimensional architectures through the successive stacking and bonding of through-etched foils (i.e., multilayer lamination), resulting in robust metallic microstructures fabricated from bulk material rather than deposited thin films. Furthermore, the reliance of these techniques on batch fabrication methods adapted from the microelectronics industry provides the capability for scalability and potential for low-cost high-volume manufacturing.

In this paper, we report on the design, fabrication, and characterization of bulk titanium microneedles made possible by these new micromachining techniques. The developed approach combines the benefits of bulk micromachining with the high fracture toughness and proven biocompatibility of titanium, thus creating a robust platform for low-cost drug delivery and diagnostic applications.

II. Design

In order to best leverage the advantages associated with the bulk micromachining and multilayer lamination of thin titanium foils, an in-plane microneedle configuration was chosen, as shown in Fig. 1. This enabled the length and shape of the microneedles to be easily defined via lithography and minimized the required etch times. Multilayer lamination also simplified the integration of the embedded microfluidic network by allowing for the definition of channel structures in one substrate followed by sealing through bonding with another thin foil substrate. Mechanical rigidity of the needles can be easily tailored by varying the substrate thicknesses, the width of the microfluidic channels (which are defined lithographically), and the etch depth of the lumen within the needle. The devices presented in this paper are composed of linear arrays of ten microneedles of three different lengths—500, 750, and 1000 μm—fabricated by multilayer lamination of two 25 μm titanium foil substrates. All microneedles are 100 μm wide with a tip taper angle of 60°.

Two-dimensional finite-element simulations (COMSOL Multiphysics 3.2, COMSOL, Inc., Burlington, MA) were used to optimize the embedded microfluidic network design to minimize inlet pressure and ensure uniform flow distribution to each microneedle in the array. Using these numerical simulations, each channel width was varied and optimized such that the volumetric flow rate delivered to each microneedle was equal to within 1%. An exact replica of this geometry was then used to microfabricate the embedded microfluidic networks. As discussed above, 25 μm foils were used in the fabrication of the devices, thereby limiting the maximum lumen etch depth to 15 μm to ensure mechanical rigidity of the needles. In order

Manuscript received June 2, 2006; revised November 20, 2006. This work was supported by DARPA-MTO. Subject Editor M. Wong.

The authors are with the Department of Mechanical and Environmental Engineering, University of California, Santa Barbara, CA 93106-5070 USA (e-mail: eparker@engineering.ucsb.edu; mprao@engineering.ucsb.edu; turner@engineering.ucsb.edu; meinhart@engineering.ucsb.edu; nmacd@engineering.ucsb.edu).

Digital Object Identifier 10.1109/JMEMS.2007.892909

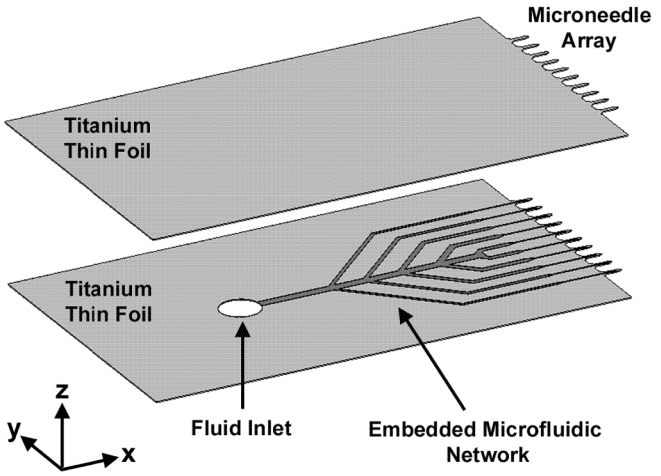

Fig. 1. Schematic showing the design concept of the bulk micromachined titanium microneedle device. Two titanium thin foils are bonded together to form microneedle arrays with embedded microfluidic networks.

to maximize volumetric throughput and minimize pressure, the inlet channel was designed to be 250 μm wide. Considering this geometry and assuming a volumetric flow rate of 100 μL/min, the corresponding Reynolds number based on the hydraulic diameter is approximately $\mathrm{Re} = 12$. Since the flow is unidirectional, and at relatively low Reynolds number, it can be described by the Stokes equation

$$-\nabla p + \mu \nabla^2 \mathbf{u} + \mathbf{F} = 0 \tag{1}$$

where p is pressure, μ is the dynamic viscosity, $\mathbf{u}$ is the fluid velocity vector, and $\mathbf{F}$ is the body force vector. Assuming the out-of-plane thickness t is much thinner than the in-plane dimension, the in-plane velocity components (u, v) are approximately parabolic in the z-direction and can be described as a so-called Hele–Shaw flow

$$u = \frac{-t^2}{8\mu}\frac{\partial p}{\partial x}\left[1 - \left(\frac{2z}{t}\right)^2\right]$$
$$v = \frac{-t^2}{8\mu}\frac{\partial p}{\partial y}\left[1 - \left(\frac{2z}{t}\right)^2\right]. \tag{2}$$

The depth-wise average velocity $\bar{u}, \bar{v}$ can be obtained by integrating (2) in the z-direction and dividing by the thickness t, yielding

$$\bar{u} = \frac{-t^2}{12\mu}\frac{\partial p}{\partial x}$$
$$\bar{v} = \frac{-t^2}{12\mu}\frac{\partial p}{\partial y}. \tag{3}$$

Since the out-of-plane direction is on the order of 15 μm and the in-plane direction is on the order of several hundred micrometers, it is convenient to simulate numerically the in-plane flow while modeling the effect of the out-of-plane direction using the Hele–Shaw solution. This can be accomplished by equating the body force to the pressure gradient created by the Hele–Shaw solution, such that

$$F_x = \frac{\partial p}{\partial x} = \frac{-12\mu}{t^2}\bar{u}$$
$$F_y = \frac{\partial p}{\partial y} = \frac{-12\mu}{t^2}\bar{v}. \tag{4}$$

The average in-plane velocity can then be estimated using a two-dimensional simulation, solving

$$-\frac{\partial p}{\partial x} + \mu\left[\frac{\partial^2}{\partial x^2} + \frac{\partial^2}{\partial y^2}\right]\bar{u} + F_x = 0$$
$$-\frac{\partial p}{\partial y} + \mu\left[\frac{\partial^2}{\partial x^2} + \frac{\partial^2}{\partial y^2}\right]\bar{v} + F_y = 0$$
$$\frac{\partial \bar{u}}{\partial x} + \frac{\partial \bar{v}}{\partial y} = 0. \tag{5}$$

The numerical simulation was conducted using a two-dimensional triangle mesh with approximately 13 000 mesh elements and 65 000 degrees of freedom. The simulation assumed a uniform inlet velocity profile.

Additional considerations that contributed to the microfluidic network design included a) use of a single fluid inlet to simplify coupling to external fluidic connections; b) limitation of the maximum channel width to 250 μm to ensure that the structure would not collapse during the bonding step; and c) avoidance of dense packing and maximization of bond area to ensure mechanical and fluidic integrity of the device.

III. Fabrication

The process flow for the fabrication of the titanium microneedle array is shown in Fig. 2. Prior to beginning the process, the thin titanium foils (2.5×2.5 cm^2 commercially pure (99.6%) Grade 1 titanium, Goodfellow Corporation, Devon, PA) were chemically mechanically polished (CMP) to facilitate lithographic patterning. Following CMP, a TiO_2 masking layer was sputter deposited (Endeavor 3000 Cluster Sputter Tool, Sputtered Films, Santa Barbara, CA; 10 sccm O_2, 20 sccm Ar, and 2300 W power) on both the front and back side of the first foil and patterned on the front side to define the external geometry of the microneedles. This oxide patterning was performed using a CHF_3 dry etch (Panasonic E640-ICP Dry Etching System, Panasonic Factory Solutions, Osaka, Japan; 500 W ICP source power, 400 W sample RF power, 1 Pa pressure, and 40 sccm CHF_3). A second lithography step was then used to define the microfluidic networks within the needle arrays. This pattern was partially transferred into the masking oxide by dry etching. Next, an anisotropic titanium deep etch was used to etch approximately halfway into the depth of the thin foil surrounding the needle array. The titanium deep etch uses a Cl_2/Ar chemistry, as described in [25]. This deep etch was followed by an oxide etch to clear the remaining masking oxide within the microfluidic network pattern. Finally, a second titanium deep etch was used to completely through-etch the titanium foil surrounding the microneedle array and define the depth of the channels. This series of etches can be performed consecutively in the same ICP etch tool (Panasonic E640-ICP

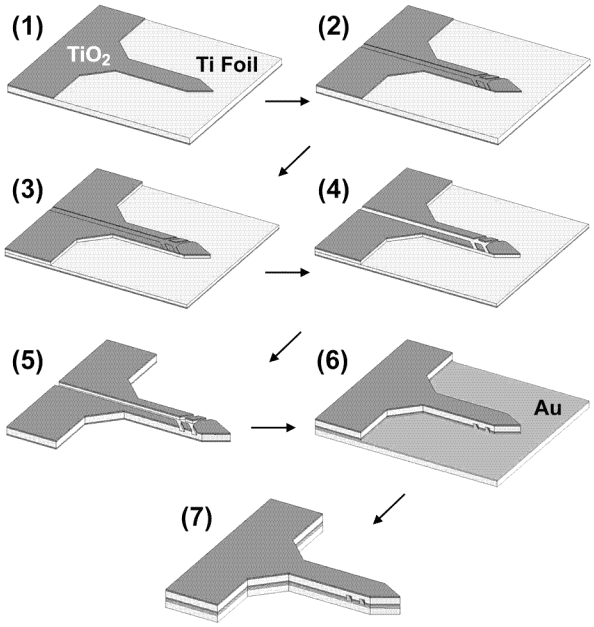

Fig. 2. Schematic outlining the bulk titanium microneedle process flow: (1) first oxide etch to define external needle geometry; (2) second oxide etch to partially define embedded channel pattern into the depth of the mask oxide; (3) first titanium deep etch partially into the titanium substrate; (4) third oxide etch to clear oxide from floor of embedded channel pattern; (5) second titanium deep etch through the remaining thickness of the titanium substrate, which also simultaneously defines the depth of the embedded channels; (6) gold thermocompression bonding to unpatterned foil (top foil has been flipped in the schematic); and (7) final titanium deep etch through the thickness of the lower foil substrate using the upper substrate as an etch mask.

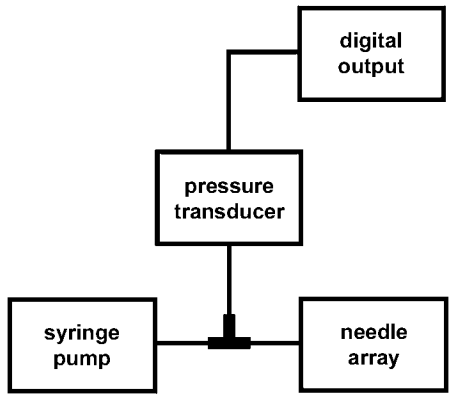

Fig. 3. Schematic diagram of the pressure testing apparatus. The volumetric flow rate is controlled by the syringe pump and the inlet pressure is measured using the transducer.

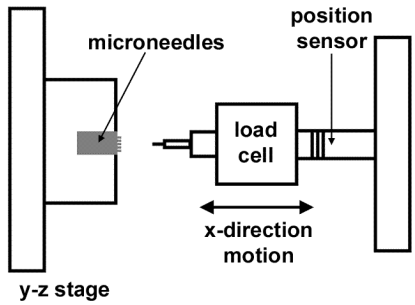

Fig. 4. Diagram of the uniaxial compression testing apparatus used to experimentally measure critical buckling loads as a function of displacement.

dry etching system) without breaking vacuum, thereby reducing process time considerably. After the needle structure was fully defined in the first foil, a 0.5-μm-thin gold layer was deposited using either sputtering or electron beam evaporation. A gold film of equal thickness was also deposited on a second unpatterned foil. These foils were then bonded together in order to seal the microfluidic networks using thermocompression bonding (SUSS Microtec SB6e substrate bonder, SUSS Microtec Inc., Santa Clara, CA; 1000 mBar tool pressure, 350 °C bond temperature, chamber pressure $\leqslant 10^{-3}$ torr, 30 min). The first foil, with the backside TiO_2 film now facing up, was then used as a mask to through-etch the second foil in a final titanium deep etch step.

IV. Experimental

Measurements of the inlet pressure as a function of the volumetric flow rate through the microneedles were used to characterize the microfluidic performance of the devices. As shown schematically in Fig. 3, the testing apparatus was composed of a pressure transducer (Validyne variable reluctance pressure transducer, 2200 kPa full scale, Validyne Engineering, Northridge, CA) connected in-line between a syringe pump (Harvard Apparatus PHD 2000 programmable syringe pump, Harvard Apparatus, Holliston, MA) and a microneedle device. All components were connected by plastic tubing, and the tubing was coupled to the microneedle device via epoxy. For most experiments, pressures were measured at flow rates between 5 and 200 μL/min. However, in order to determine the critical pressure at which the thermocompression bond fails, the volumetric flow rate was continually increased beyond this range until failure occurred, as evidenced by a sudden drop in the measured inlet pressure.

Micromechanical testing was used to characterize microneedle buckling behavior under uniaxial compression, thus simulating conditions similar to those encountered during skin insertion. This testing was performed using the apparatus shown schematically in Fig. 4. The microneedle devices were secured to a y-z translation stage, which enabled alignment of the needles with the loading apparatus. The loading apparatus was composed of a machined flat punch that was narrow enough to allow probing of individual needles in the array. This punch was mounted to a load cell (Sensotec load cell, 2.5 N full scale, Honeywell Sensotec, Columbus, OH), which was mounted to the actuator head of the load frame. The load response of each individual microneedle was recorded as a function of uniaxial compressive displacement of the actuator under displacement control conditions (crosshead speed $\sim$5.5 μm/s). Both single-foil (i.e., no embedded microfluidics) and bonded dual-foil devices with 500, 750, and 1000 μm microneedles were tested in this fashion. Testing of the single foil-based needles was performed to validate the loading apparatus function and provide insight into the appropriate end conditions for use in the finite-element simulations of the buckling response. Testing of the bonded dual foil devices was performed to evaluate the effect of the bonded interface on the buckling behavior. For each test, a maximum displacement stroke of

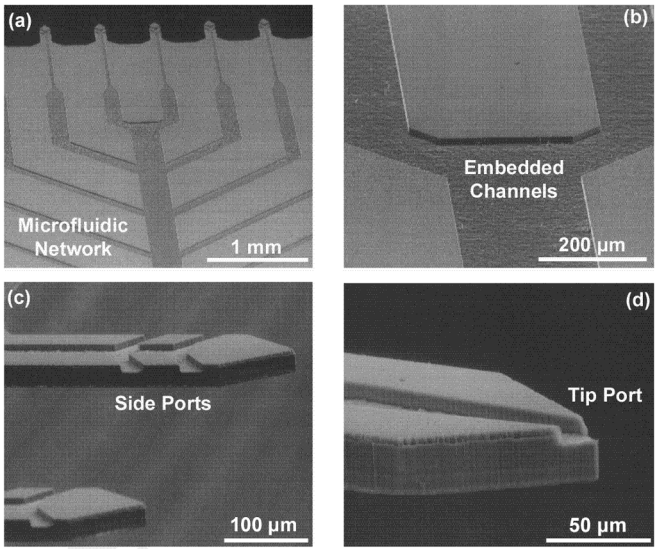

Fig. 5. SEMs of the embedded microfluidic network defined in the first foil substrate prior to thermocompression bonding of the second foil. The titanium thin foil substrate is 25 μm thick, and the channel depth is approximately 10 μm.

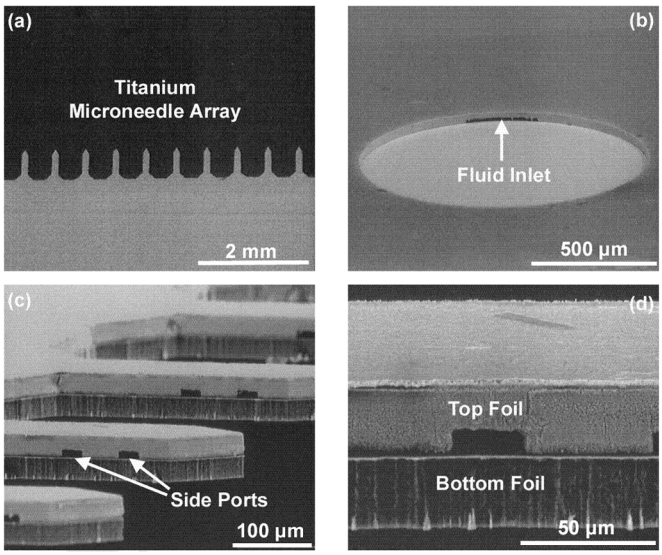

Fig. 6. SEMs of a completed microneedle device comprised of two bonded 25 μm titanium thin foils. All microneedles in the shown array are 500 μm long and 100 μm wide.

approximately 150 μm was used to ensure displacement well into the buckled regime.

V. Results and Discussion

Fig. 5 shows several scanning electron microscope (SEM) images of a single through-etched foil with embedded microfluidic networks prior to thermocompression bonding of the second titanium foil. Fig. 6 shows the completed titanium microneedle array once the second foil has been bonded to seal the embedded channel network. Although the current channel architecture is relatively simplistic, the potential for integration of arbitrarily complex two-dimensional microfluidic networks with the current design concept is clearly apparent. It should also be noted

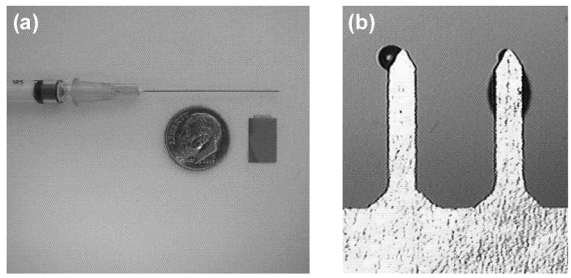

Fig. 7. (a) Comparison of the relative sizes of a 25-gauge 1.5-in hypodermic needle, a U.S. dime coin piece, and a titanium device composed of an array of ten 750 μm microneedles. (b) Optical microscopy-based visualization of fluidic throughput by 750 μm microneedles with tip ports.

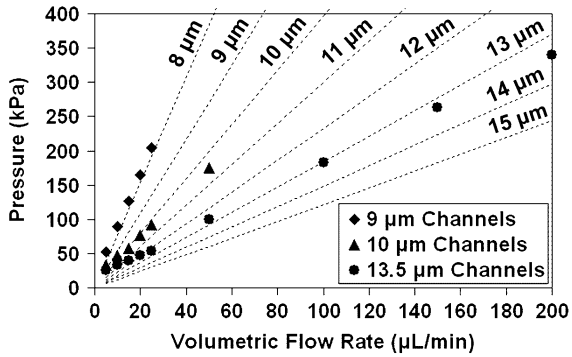

Fig. 8. Plot of pressure versus inlet volumetric flow rate for 500-μm-long microneedle devices with varying embedded channel depths. Actual channel depths were measured using optical profilometry. Dashed lines represent simulated pressure values at varying channel depths. Numerical simulations were used to optimize each channel width such that the volumetric flow rate delivered to each microneedle was equal to within 1%.

that the current design concept enables decoupling of the mechanical and fluidic performance of the device, thus simplifying optimization considerably. For example, needle shank stiffness can be easily increased without affecting flow rate or inlet pressure through use of thicker substrates and/or wider shanks. Similarly, flow rate can be increased without increasing inlet pressure or reducing stiffness by simply using thicker substrates and more deeply etched channels.

Fig. 7(a) shows the considerably smaller size of the titanium microneedles relative to a conventional small gauge hypodermic needle. Although beyond the scope of this paper, others have shown that needles with somewhat comparable dimensions are able to penetrate the skin with little to no sensation of pain [26]. Fig. 7(b) shows a demonstration of the fluidic throughput capability of the device by microneedles with tip ports.

Fig. 8 shows the variation of inlet pressure for a set of 500 μm microneedle devices as a function of flow rate and embedded channel depth. The experimental results are observed to agree fairly well with the finite-element simulations and show the expected trends of increasing inlet pressure with increasing flow rate and decreasing channel depth. Higher flow rate testing of samples with channel depths similar to those tested for Fig. 8 revealed that the average maximum achievable pressure prior to failure of the bonded interface was 272 ± 88 kPa for ten tested specimens, with a minimum recorded value of 179 kPa and a maximum of 422 kPa.

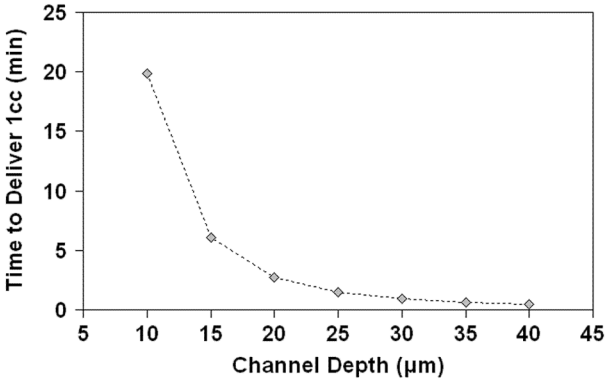

Fig. 9. Plot of finite-element-based predictions of delivery time for 1 cc of water at room temperature for varying microneedle embedded channel depths. The maximum possible volumetric flow rates were computed for different channel depths assuming a nominal inlet pressure of 200 kPa, which is 25% below the average bond delamination pressure.

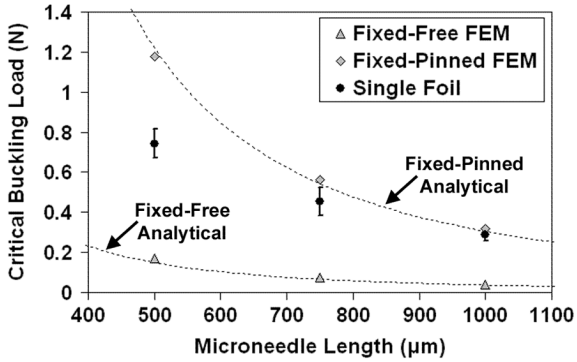

Fig. 10. Plot of critical buckling load versus microneedle length for 25-μm-thick single foil-based devices with needle lengths of 500, 750, and 1000 μm. Solid data points represent the average measured buckling load for 20 specimens with the standard deviation represented by the associated error bars. Dashed lines and shaded points represent analytical and finite element solutions, respectively, assuming either fixed-free or fixed-pinned end loading conditions.

Results from finite-element simulations shown in Fig. 9 indicate that the current microneedle devices are more than capable of delivering clinically relevant fluid volumes ($\sim$1 cc) at inlet pressures well below the average delamination pressure. Moreover, the simulations show that delivery times can be reduced considerably by increasing channel depth beyond the current maximum of 15 μm. This would, however, require use of thicker foils to ensure sufficient mechanical rigidity.

While the measured bond failure pressures have been found to be sufficient for the current device requirements, these values are lower than those reported by other studies on gold thermocompression bonding [27], [28]. This discrepancy could be caused by a number of factors, including differences in a) gold deposition methods and conditions; b) thermocompression bonding procedures and conditions; and/or c) bond strength testing procedures and conditions. The relatively high surface roughness of the titanium foils used in this paper ($R_A \sim 25$ nm root mean square) could also be a contributing factor due to the potential reduction of effective bonding surface area caused by asperity contact. Improvements in the bond strength are therefore certainly possible with further optimization but beyond the scope of this paper.

As discussed earlier, buckling-induced bending is predicted to be the primary mechanical failure mode during microneedle insertion. The critical load $P_{\rm cr}$ upon which such failures will occur can be estimated by the following:

$$P_{\rm cr} = \frac{\pi^2 E I_z}{(KL)^2} \tag{7}$$

where E is the modulus of elasticity, I_z is the second-area moment of inertia, and K is defined by the boundary conditions. For the current studies, two end conditions and their corresponding K values were considered, both fixed-free $(\mathrm{K} = 2)$ and fixed-pinned $(\mathrm{K} = 0.699)$ [29], [30]. However, the sharply pointed tip geometry of the current microneedle devices deviates from the idealized flat-ended column geometry assumed in (6); thus finite-element modeling was also employed to ensure more accurate buckling load predictions (COMSOL Multiphysics 3.2, COMSOL, Inc., Burlington, MA). Upon comparison, the analytical and finite-element solutions were found to be in good agreement.

Fig. 10 shows the experimentally measured critical buckling load for single foil-based microneedles with lengths ranging from 500 to 1000 μm, as well as the analytical and finite-element predictions for both the fixed-free and fixed-pinned geometry. As can be seen, the experimental data most closely correspond to the analytical and finite-element predictions based on the assumption of fixed-pinned boundary conditions. This is as expected due to friction at the interface between the microneedle tip and the machined flat punch of the loading apparatus. However, this agreement is observed to decrease with decreasing microneedle length. This is most likely due to the increased stiffness of the shorter needles, which provides greater lateral driving force to overcome the frictional forces that pin the needle tip.

The critical buckling loads of the bonded dual foil microneedles are shown in Fig. 11. Though the buckling loads of the dual foil microneedles were found to be higher than those of the single foil microneedles, they were well below loads predicted by analytical and finite-element methods for a fixed-pinned geometry. SEMs of buckled single and dual foil needles are shown in Fig. 12. As can be seen, considerable plastic deformation has occurred, as was expected given the large displacement stroke used during the testing. It is important to note that no cracking or fracture of the needles was observed during testing, thus highlighting the potential for fabrication of robust, damage-tolerant microneedles using titanium. Fig. 12 also shows that considerable delamination occurs at the gold–gold interface in the bonded dual-foil devices. This delamination is due to poor thermocompression bonding between the two foils and is the most likely cause of the low buckling loads observed experimentally. As discussed earlier, improvement of the bond strength is possible and would most certainly lead to higher buckling loads.

The force required for microneedle insertion has been shown to be dependent upon a number of factors, including needle geometry and dimensions, needle spacing, and insertion location (e.g., hand, forearm, etc.). While measurement of the insertion force of the titanium microneedles is beyond the scope of this

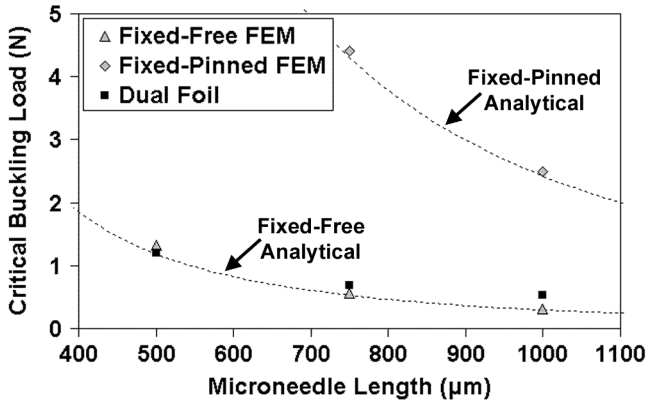

Fig. 11. Plot of critical buckling load versus microneedle length for 50-μm-thick dual-foil needles (i.e., devices composed of two 25 μm foils bonded together) for needles lengths of 500, 750, and 1000 μm. Solid data points represent the average measured buckling load for 20 specimens. The standard deviation of the buckling measurements at each microneedle length was found to be less than 0.11 N (not visible on this scale.) Dashed lines and shaded points represent analytical and finite-element solutions, respectively, assuming either fixed-free or fixed-pinned end loading conditions.

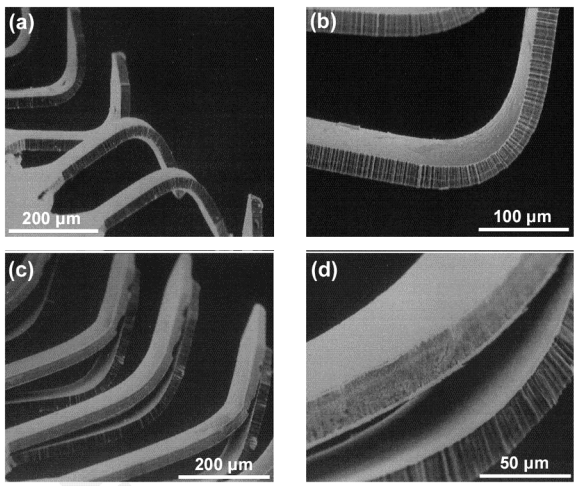

Fig. 12. SEMs of bulk titanium microneedles following uniaxial compression testing using the mechanical testing apparatus detailed in Fig. 4: (a) 500 μm single-foil microneedles tend to buckle in random directions; (b) shaft of 1000 μm single-foil microneedle shows no sign of fracture even after severe deformation; (c) 750 μm bonded dual-foil needles tend to buckle towards the top foil (foil with etched microfluidic network); and (d) buckling of the 750 μm dual-foil needles causes delamination at the gold–gold bond interface between the two foils.

paper, comparison of the observed buckling loads to the insertion forces reported for other microneedles with comparable geometry and dimensions suggest that they should withstand insertion. Using skin analogs, Chandrasekaran *et al.* [18] found insertion forces on the order of 0.07–0.1 N, while Davis *et al.* [31] measured forces on the order of 0.08–3.04 N. As seen in Fig. 12, the measured buckling loads for the current titanium microneedles range from 0.5 to 1.2 N, thus surpassing the majority of these reported insertion forces. Moreover, as discussed earlier, the buckling strength of the current microneedles could be improved further through optimization of the thermocompression bonding process and/or needle geometry (e.g., wider shanks, thicker foils, etc.), thus potentially providing even greater margins of safety. Finally, it is important to reiterate that buckling of the current titanium microneedles is characterized by a graceful failure mode (i.e., large-scale plastic deformation) as opposed to the catastrophic failure associated with buckling of more brittle materials such as silicon and glass (i.e., fracture). Coupled with the inherent biocompatibility of titanium, this provides for additional safety and reliability relative to the majority of other comparable in-plane microneedle devices reported thus far.

VI. Conclusion

Linear microneedle arrays fabricated using bulk titanium substrates were developed to address the micromechanical limitations of more traditional material systems commonly used by microneedle devices. The fabrication of devices that allow for active fluid delivery (or extraction) was enabled by recently developed titanium bulk micromachining and multilayer lamination technologies. Exploitation of these technologies also allows for decoupling of the mechanical and fluidic performance of the device, thus facilitating optimization considerably relative to other developed fabrication methods. Perhaps most importantly, the use of bulk titanium substrates eliminates fracture-induced failure common in more brittle materials while maintaining adequate mechanical rigidity. This, in conjunction with the proven biocompatibility of titanium, makes it an ideal material system for drug delivery applications.

Acknowledgment

The authors would like to thank D. Bothman and K. Fields for their assistance with design and assembly of the microfluidic and micromechanical characterization apparatus.

References

[1] D. V. McAllister, M. G. Allen, and M. R. Prausnitz, "Microfabricated microneedles for gene and drug delivery," *Annu. Rev. Biomed. Eng.*, vol. 2, pp. 289–313, 2000.

[2] M. L. Reed and W. K. Lye, "Microsystems for drug and gene delivery," *Proc. IEEE*, vol. 92, pp. 56–, 2004.

[3] J. Chen, K. D. Wise, J. F. Hetke, and S. C. Bledsoe, Jr., "A multichannel neural probe for selective chemical delivery at the cellular level," *IEEE Trans. Biomed. Eng.*, vol. 44, pp. 760–, 1997.

[4] H. Gardeniers, R. Luttge, E. J. W. Berenschot, M. J. de Boer, S. Y. Yeshurun, M. Hefetz, R. van't Oever, and A. van den Berg, "Silicon micromachined hollow microneedles for transdermal liquid transport," *J. Microelectromech. Syst.*, vol. 12, pp. 855–862, 2003.

[5] P. Griss and G. Stemme, "Side-opened out-of-plane microneedles for microfluidic transdermal liquid transfer," *J. Microelectromech. Syst.*, vol. 12, pp. 296–301, 2003.

[6] S. Henry, D. V. McAllister, M. G. Allen, and M. R. Prausnitz, "Microfabricated microneedles: A novel approach to transdermal drug delivery," *J. Pharm. Sci.*, vol. 87, pp. 922–925, 1998.

[7] L. W. Lin and A. P. Pisano, "Silicon-processed microneedles," *J. Microelectromech. Syst.*, vol. 8, pp. 78–84, 1999.

[8] E. Mukerjee, S. D. Collins, R. R. Isseroff, and R. L. Smith, "Microneedle array for transdermal biological fluid extraction and in situ analysis," *Sens. Actuators A, Phys.*, vol. 114, pp. 267–275, 2004.

[9] S. J. Paik, A. Byun, J. M. Lim, Y. Park, A. Lee, S. Chung, J. K. Chang, K. Chun, and D. D. Cho, "In-plane single-crystal-silicon microneedles for minimally invasive microfluid systems," *Sens. Actuators A, Phys.*, vol. 114, pp. 276–284, 2004.

[10] B. Stoeber and D. Liepmann, "Arrays of hollow out-of-plane microneedles for drug delivery," *J. Microelectromech. Syst.*, vol. 14, pp. 472–479, 2005.

[11] N. H. Talbot and A. P. Pisano, "Polymolding: Two wafer polysilicon micromolding of closed-flow passages for microneedles and microfluidic devices," presented at the Solid-State Sensor and Actuator Workshop, Transducers Research Foundation, Cleveland, OH, 1998, unpublished.

[12] J. D. Zahn, N. H. Talbot, D. Liepmann, and A. P. Pisano, "Microfabricated polysilicon microneedles for minimally invasive biomedical devices," *Biomed. Microdev.*, vol. 2, pp. 295–303, 2000.
[13] D. V. McAllister, P. M. Wang, S. P. Davis, J. H. Park, P. J. Canatella, M. G. Allen, and M. R. Prausnitz, "Microfabricated needles for transdermal delivery of macromolecules and nanoparticles: Fabrication methods and transport studies," *Proc. Nat. Acad. Sci.*, vol. 100, pp. 13 755–13 760, 2003.
[14] J. H. Park, M. G. Allen, and M. R. Prausnitz, "Biodegradable polymer microneedles: Fabrication, mechanics and transdermal drug delivery," *J. Control. Rel.*, vol. 104, pp. 51–66, 2005.
[15] J. Brazzle, I. Papautsky, and A. B. Frazier, "Micromachined needle arrays for drug delivery or fluid extraction—Design and fabrication aspects of fluid coupled arrays of hollow metallic microneedles," *IEEE Eng. Med. Biol. Mag.*, vol. 18, pp. 53–58, 1999.
[16] J. D. Brazzle, I. Papautsky, and A. B. Frazier, "Hollow metallic micromachined needle arrays," *Biomed. Microdev.*, vol. 2, pp. 197–205, 2000.
[17] S. Chandrasekaran, J. D. Brazzle, and A. B. Frazier, "Surface micromachined metallic microneedles," *J. Microelectromech. Syst.*, vol. 12, pp. 281–288, 2003.
[18] S. Chandrasekaran and A. B. Frazier, "Characterization of surface micromachined metallic microneedles," *J. Microelectromech. Syst.*, vol. 12, pp. 289–295, 2003.
[19] S. P. Davis, W. Martanto, M. G. Allen, and M. R. Prausnitz, "Hollow metal microneedles for insulin delivery to diabetic rats," *IEEE Trans. Biomed. Eng.*, vol. 52, pp. 909–915, 2005.
[20] I. Papautsky, J. Brazzle, H. Swerdlow, R. Weiss, and A. B. Frazier, "Micromachined pipette arrays," *IEEE Trans. Biomed. Eng.*, vol. 47, pp. 812–819, 2000.
[21] L. A. Garner, "Contact dermatitis to metals," *Dermatol. Therapy*, vol. 17, pp. 321–, 2004.
[22] D. M. Brunette, P. Tengvall, M. Textor, and P. Thomsen, *Titanium in Medicine: Material Science, Surface Science, Engineering, Biological Responses and Medical Applications*. Berlin, Germany: Springer, 2001.
[23] R. V. Noort, "Titanium: The implant material of today," *J. Mater. Sci.*, vol. 22, pp. 3801–3811, 1987.
[24] M. F. Aimi, M. P. Rao, N. C. Macdonald, A. S. Zuruzi, and D. P. Bothman, "High-aspect-ratio bulk micromachining of titanium," *Nature Mater.*, vol. 3, pp. 103–105, 2004.
[25] E. R. Parker, B. J. Thibeault, M. F. Aimi, M. P. Rao, and N. C. MacDonald, "Inductively coupled plasma etching of bulk titanium for MEMS applications," *J. Electrochem. Soc.*, vol. 152, pp. C675–C683, 2005.
[26] S. Kaushik, A. H. Hord, D. D. Denson, D. V. McAllister, S. Smitra, M. G. Allen, and M. R. Prausnitz, "Lack of pain associated with microfabricated microneedles," *Anesth. Analg.*, vol. 92, pp. 502–504, 2001.
[27] M. M. V. Taklo, P. Storas, K. Schjolberg-Henriksen, H. K. Hasting, and H. Jakobsen, "Strong, high-yield and low-temperature thermocompression silicon wafer-level bonding with gold," *J. Micromech. Microeng.*, vol. 14, pp. 884–890, 2004.
[28] C. H. Tsau, S. M. Spearing, and M. A. Schmidt, "Characterization of wafer-level thermocompression bonds," *J. Microelectromech. Syst.*, vol. 13, pp. 963–, 2004.
[29] R. G. Budynas, *Advanced Strength and Applied Stress Analysis*. Boston, MA: McGraw-Hill, 1999.
[30] A. C. Ugural and S. K. Fenster, *Advanced Strength and Applied Elasticity*. Upper Saddle River, NJ: Pearson, 1995.
[31] S. P. Davis, B. J. Landis, Z. H. Adams, M. G. Allen, and M. R. Prausnitz, "Insertion of microneedles into skin: Measurement and prediction of insertion force and needle fracture force," *J. Biomech.*, vol. 37, pp. 1155–1163, 2004.

E. R. Parker, photograph and biography not available at the time of publication.

M. P. Rao, photograph and biography not available at the time of publication.

K. L. Turner, photograph and biography not available at the time of publication.

C. D. Meinhart, photograph and biography not available at the time of publication.

N. C. MacDonald, photograph and biography not available at the time of publication.